nature communications

Article

https://doi.org/10.1038/s41467-024-54406-8

Holistic numerical simulation of a quenching process on a real-size multifilamentary superconducting coil

Received: 5 April 2024

Accepted: 10 November 2024

Published online: 01 December 2024

Check for updates

Cun Xue[1] ✉, Han-Xi Ren[2], Peng Jia[1], Qing-Yu Wang[2], Wei Liu[3], Xian-Jin Ou[4,5], Liang-Ting Sun[4,7] & Alejandro V. Silhanek[6]

Superconductors play a crucial role in the advancement of high-field electromagnets. Unfortunately, their performance can be compromised by thermomagnetic instabilities, wherein the interplay of rapid magnetic and slow heat diffusion can result in catastrophic flux jumps, eventually leading to irreversible damage. This issue has long plagued high-J_c Nb_3Sn wires at the core of high-field magnets. In this study, we introduce a large-scale GPU-optimized algorithm aimed at tackling the complex intertwined effects of electromagnetism, heating, and strain acting concomitantly during the quenching process of superconducting coils. We validate our model by conducting comparisons with magnetization measurements obtained from short multifilamentary Nb_3Sn wires and further experimental tests conducted on solenoid coils while subject to ramping transport currents. Furthermore, leveraging our developed numerical algorithm, we unveil the dynamic propagation mechanisms underlying thermomagnetic instabilities (including flux jumps and quenches) within the coils. Remarkably, our findings reveal that the velocity field of flux jumps and quenches within the coil is correlated with the cumulated Joule heating over a time interval rather than solely being dependent on instantaneous Joule heating power or maximum temperature. These insights have the potential to optimize the design of next-generation superconducting magnets, thereby directly influencing a wide array of technologically relevant and multidisciplinary applications.

Due to high current carrying capability with loss-less characteristics, superconductors are essential components for the development of high-field electromagnets. However, their performance can be threatened by thermomagnetic instabilities. The interplay between swift flux motion and slow heat diffusion gives rise to sudden flux bursts, which limit the lifetime of the coil. Indeed, frequent magnetic flux jumps had been identified as a long-standing issue[1–9] at the source of serious problems in high-J_c Nb_3Sn wires/strands used in 10–16 T magnets[10] and over-20 T hybrid magnets[11]. Previous reports have shown that flux jumps may cause premature quenches at low fields and currents well below the designed operating regime[12–15]. In this case, a rather lengthy, helium-intensive, and expensive process of magnet

[1]School of Mechanics, Civil Engineering and Architecture, Northwestern Polytechnical University, 710072 Xi'an, China. [2]School of Aeronautics, Northwestern Polytechnical University, 710072 Xi'an, China. [3]Western Superconducting Technologies Co., Ltd., and Xi'an Superconducting Magnet Technology Co. Ltd, 710014 Xi'an, China. [4]Institute of Modern Physics, Chinese Academy of Sciences, 730000 Lanzhou, China. [5]School of Nuclear Science and Technology, University of Chinese Academy of Sciences, 100049 Beijing, China. [6]Q-MAT | Experimental Physics of Nanostructured Materials (EPNM), Department of Physics, University of Liege (ULiege), B5a, 4000 Liège, Belgium. [7]Present address: School of Nuclear Science and Technology, University of Chinese Academy of Sciences, 100049 Beijing, China. ✉e-mail: xuecun@nwpu.edu.cn

training is needed in order to achieve the targeted maximum field and ramp rate[16]. Additionally, the stochastic behavior of magnetic flux jumps significantly affects the field stability in the magnet bore and makes accurate field-correction protocols particularly challenging[17,18]. Furthermore, prevention measures via quench detection systems based on voltage spikes seem to be prone to errors[17,19].

Soon after magnetic flux jumps were first observed and investigated in the 1960s[20], the underlying physical mechanism was revealed[21–28] along with the relevant physical parameters (temperature[29], ramping rate[30], sample size[31], border defects[32]) ruling the nucleation and growth of thermomagnetic instabilities. For composite superconducting wires/strands, early criteria for triggering magnetization flux jumps were proposed by Swartz and Bean[23] and Wilson[33]. Subsequently, a series of studies were carried out to describe the characteristics of low-field flux jumps in order to develop a new generation of Nb_3Sn high-field magnets[34–38]. It was found that reducing the effective filament size and improving the residual resistivity ratio (RRR) is of paramount importance for suppressing flux jumps[35,39,40]. Even though initial efforts have been directed to single superconducting wires and criteria have been established by general electromagnetic analysis in limited cases of adiabatic or isothermal assumptions, the last decade has witnessed steady progress in understanding the more complex multifilamentary strands[41–48]. Recently, Xu et al. investigated the influence of heat treatment temperature and Ti-doping on flux jumps and demonstrated that introducing high-specific heat substances can improve the stability of Nb_3Sn wires[49,50].

Unfortunately, the theoretical development for a single wire is not adequate to describe complex coils due to the distinct characteristics of the latter. Namely, (i) Different wires in the coil are generally exposed to magnetic fields with different ramp rates. (ii) Wires in a coil are not isolated but rather represent complex correlated systems. (iii) The stability of each wire strongly depends on its time-dependent electromagnetic penetration as well as the thermal shock from neighboring wires during the occurrence of localized flux jumps (see details in Supplementary Note 1). Consequently, criteria for determining the onset of flux jumps which are accurate for an isolated single wire, may not be applicable to a coil consisting of correlated wires. To date, there are not sufficiently powerful tools based on numerical algorithms or available commercial software able to deal with correlated systems such as those of technologically relevant coils typically involving thousands of multifilamentary wires. In this context, multiscale design from filament to global structure for magnets is still considered a daunting, if not impossible, task.

As a matter of fact, numerical simulations of the thermomagnetic instabilities leading to partial flux jumps or complete quenching of a full-sized coil represent a formidably complex quest for several reasons. Firstly, the relation between electric field E and current density J exhibits a very strong nonlinear dependence caused by the intricate flux dynamics involving enormous amounts of nanoscale superconducting vortices. Secondly, the superconducting coils require a multiphysics approach that includes an interplay of heat diffusion, electromagnetic response, and mechanical strain. Thirdly, unlike single-phase superconducting samples (either in bulk or film form), the multiscale structures of magnets containing microfilaments, millimetric wires, and metric coils as shown in Fig. 1 cannot be simulated through homogenization methods. Last, but not least, the thermal conductivity of copper is 3–4 orders of magnitude larger than that of the epoxy. Since the dynamics of thermomagnetic instabilities rely on accurate temperature field calculations, it is impossible to obtain a satisfactory result for a composite coil simply by homogenization method with equivalent thermal parameters.

In this work, we develop an unprecedented large-scale GPU-advanced algorithm to address the aforementioned intractable problems of superconducting coils. We validate the numerical algorithm by comparing it with a series of experiments involving magnetization measurements on short multifilamentary Nb_3Sn and MgB_2 wires as well as experimental tests performed on solenoid coils under different conditions. Moreover, utilizing the developed numerical algorithm, we unveil the dynamic propagating processes of thermomagnetic instabilities (flux jumps and quenches) in the coils. Surprisingly, we demonstrate that the velocity field of flux jumps and quenches in the coil results from the quantity of Joule heating released in each wire over a time interval rather than the instantaneous value and the maximum temperature at triggering time. These results may provide the necessary breakthrough to optimize the design of next-generation superconducting magnets, which has a direct impact on technologically relevant and multidisciplinary applications.

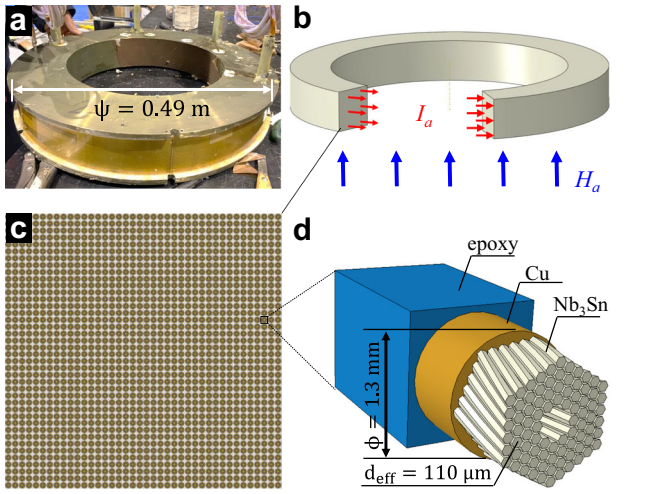

Fig. 1 | Operational superconducting magnet and numerical model. a Solenoid superconducting magnet fabricated to benchmark against the numerical calculations. The solenoid consists of 1558 densely wound turns of high-J_c Nb_3Sn wire with 84 sub-elements fabricated by internal-tin process (see details in Supplementary Note 3). **b** Schematic of a solenoid coil exposed to a ramping transport current I_a and a ramping external magnetic field H_a. **c** and **d** Cross-section of the solenoid coil with a zoom on the composite multifilamentary Nb_3Sn wire.

Results

Validation of the numerical algorithm on single multifilamentary wires

Figure 2a and b shows the numerical algorithm for the electromagnetic responses of a superconducting solenoid coil wound with multifilamentary wires (see details in the "Methods" section and Supplementary Note 4). We first compare the electromagnetic response obtained by our 2D numerical model with the results obtained by the 3D twisting model with a helicoidal structure (see details in Supplementary Note 5). We will demonstrate that our 2D numerical model can capture the main characteristics of twisted multifilamentary wires and provide a very good approximation to study the electromagnetic response in the cases of external magnetic fields with low field ramp rates or low frequencies. The error on computed AC losses is less than 3% when the ramp rate of the applied magnetic field remains below 50 mT/s. In order to further validate our 2D numerical algorithm, as shown in Fig. 2c, we carry out experimental measurements on short samples of internal-tin Nb_3Sn wires exposed to a cycling transversal magnetic field (±3 T) with a sweeping rate of 10 mT/s at 4.2 K. Figure 2d shows the dependence of J_c on magnetic field at various temperatures for a commercial superconducting wire from Oxford Superconducting Technology (OST) as obtained by experiments (see details in Supplementary Note 2). As shown in Fig. 2e and further discussed in Supplementary Note 6, it can be found that the simulated magnetization loops for both OST and Western Superconductor Technologies (WST)

https://doi.org/10.1038/s41467-024-54406-8

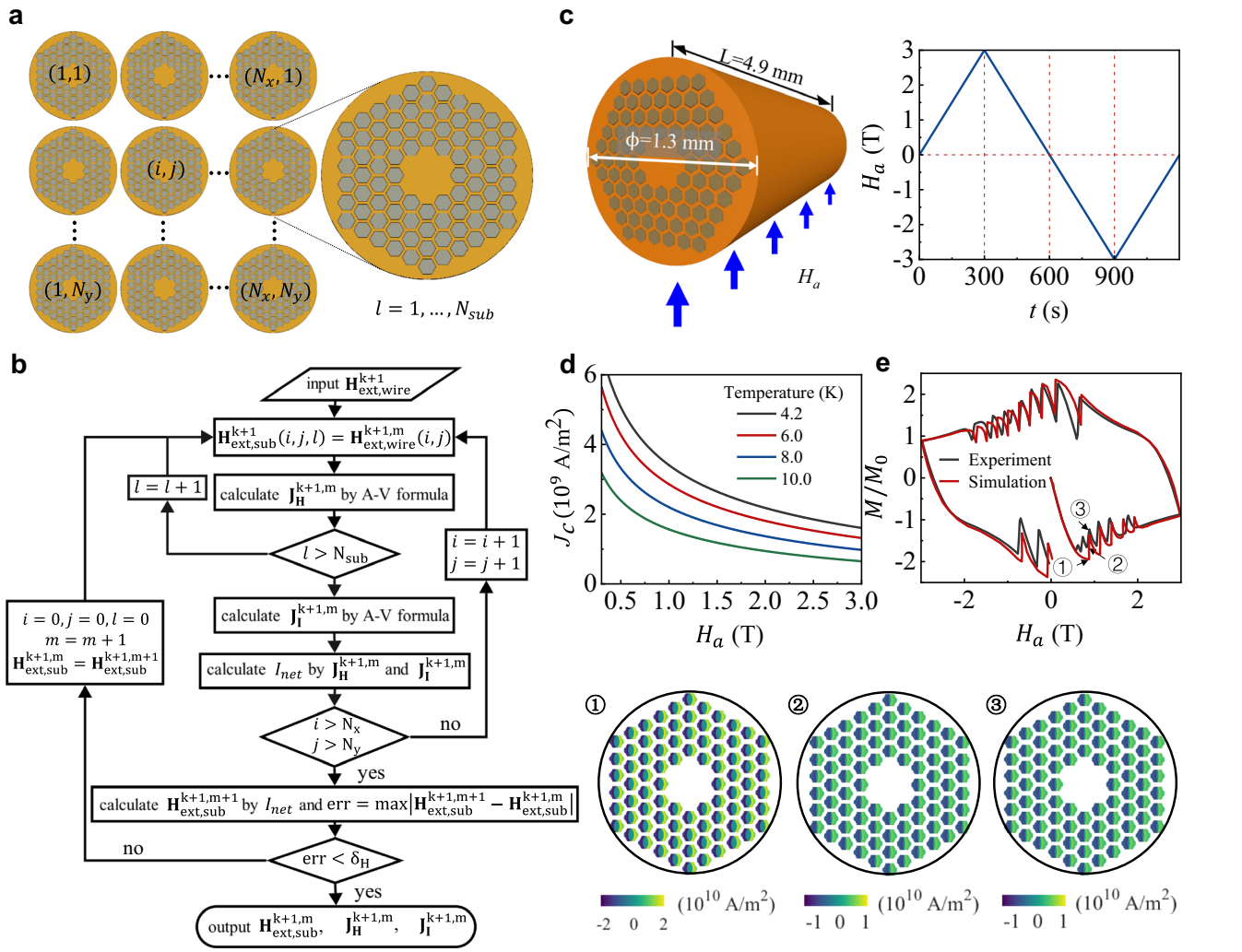

Fig. 2 | Large-scale GPU-advanced algorithm for a superconducting coil. **a** Modeled system consisting of a superconducting coil with $N_x \times N_y$ turns. Each wire contains N_{sub} sub-elements. **b** Flow chart for the key subroutine in the numerical algorithm performed on the graphics processing unit (GPU) to simulate the nucleation, growth, and damping of thermomagnetic instabilities (flux jumps and quenches) in the superconducting coils. The flow chart for the main program can be seen in Supplementary Note 4. **c** Schematic of the short segment of Nb_3Sn wire used to collect experimental measurements and exposed to an applied magnetic field $H_a(t)$ (see details in Supplementary Note 3). **d** Experimentally determined critical current density J_c as a function of magnetic field H_a for various temperatures. **e** Experimental and simulated magnetization of the Nb_3Sn short segment wire exposed to a transverse magnetic field loop with the sweeping rate of 10 mT/s at 4.2 K. The lower panels labeled from left to right 1, 2, and 3 represent the simulated current density distributions during a flux jump for the magnetic fields indicated in the hysteresis loop shown in (**e**).

wires agree well with the experimental results, which provides compelling evidence validating our numerical algorithm. Additionally, both experiments and simulations show that the magnetization of the Nb_3Sn wire does not decrease to zero during the flux jumps, suggesting that the temperature does not exceed the superconducting critical temperature T_c during partial flux jumps. Nevertheless, the current density decreases significantly during this process (see lower panels of Fig. 2e).

Moreover, our numerical algorithm can be used to investigate not only the low-temperature multifilamentary superconducting wires (NbTi and Nb_3Sn) but also high-temperature superconducting wires with similar structures, such as multifilamentary MgB_2 wires and Bi2212 wires. In particular, MgB_2 wires[51–54] are currently investigated in low-loss coils of next-generation superconducting rotating machines. Supplementary Note 7 shows that the simulated magnetization versus magnetic field for the multifilamentary MgB_2 wire agrees well with the experiments, providing additional validation to our numerical algorithm.

Flux jump propagation in a magnetic coil

Encouraged by the success of the proposed numerical algorithm on single multifilamentary wires, we then explored the flux jumps in a solenoid coil with 1600 (40 × 40) turns of Nb_3Sn wires. The upper panel of Fig. 3a shows the experimentally observed voltage signal exhibiting frequent flux jumps during a continuous current ramp of 0.5 A/s for the OST solenoid coil. Because of the complexity of the circuits in the actual coil's measurement system, the experimental voltage caused by flux jumps is obtained as a relative quantity. Therefore, the voltage per unit of length (i.e., the electric field) shown in Fig. 3a is normalized by its maximum value. Due to the fact that J_c of Nb_3Sn is very sensitive to strain, this effect should also be taken into consideration in the numerical simulations. The mechanical response of the solenoid coil includes three parts: thermal strain caused by cooling down to 4.2 K, pre-strain process caused by the compression of the aluminum strip, and the electromagnetic strain produced by the Lorentz force. Detailed analyses of the mechanical deformation and $J_c(\varepsilon)$ are shown in Supplementary Notes 2 and 10.

https://doi.org/10.1038/s41467-024-54406-8

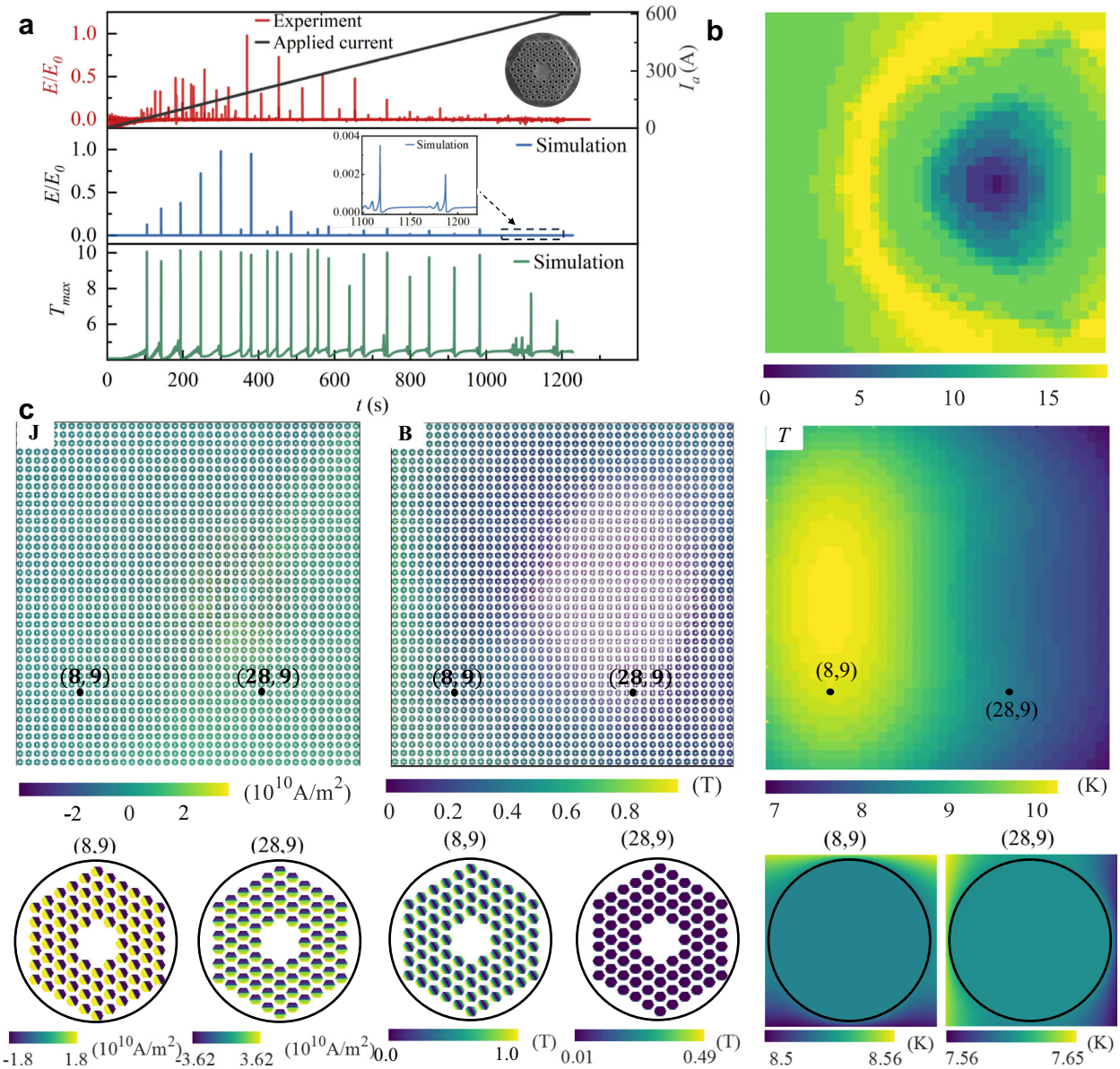

Fig. 3 | Flux jumps during the ramping process of a superconducting solenoid coil. a The upper panel shows the variations of applied current with time and voltage (or electric field) peaks caused by flux jumps (normalized by its maximum value) for the solenoid coil with OST Nb_3Sn wires (84 sub-elements). The middle and lower panels (normalized by their maximum value) show the time evolution of simulated voltage (or electric field) peaks caused by flux jumps and the maximum temperature in the coil, respectively. **b** Contour plot indicating the number of flux jumps for each wire during the ramping process. **c** The simulated current density, magnetic field, and temperature during the second flux jump. The lower panels show detailed views for two wires with coordinates (8, 9) and (28, 9).

As shown in Fig. 3a, the main features associated with the presence of flux jumps are also observed in the experiments, including the onset time and end time of the flux jumps. Additionally, the simulated results show that the voltage peaks caused by flux jumps first increase and then decrease with increasing the applied current, which is consistent with the experiments. As shown in Supplementary Note 11, we carry out more experiments and perform additional numerical simulations under several different conditions. Our numerical simulations reproduce general features associated with flux jumps similar to those observed in the experiments. Considering the fact that real Nb_3Sn wires may be inhomogeneous on different cross-sections of the coil, it is not surprising that a perfect time-matching of the occurrence of flux jump events is not observed. As shown in Fig. S30 of Supplementary Note 11, the wire's non-uniformity can indeed impact the details of flux jump occurrence with increasing applied current. However, it does not affect the main characteristics of flux jumps. Additionally, quantitative validation of the voltage induced by flux jumps obtained from the numerical algorithm by a specifically manufactured small coil can be found in Supplementary Note 11. Therefore, we can safely state that various experiments correctly validate the numerical algorithm for coils. Figure 3b shows the number of flux jumps across the entire coil during the ramping process. The statistics of the flux jumps in each wire during this process reveal that flux jumps are not triggered uniformly in all wires. The thermomagnetic instabilities are statistically less likely to occur in the center of the region on the right side. This is because the ramp rate of the local magnetic field in this region is substantially smaller than elsewhere. Figure 3c shows snapshots of the current density, the magnetic field distributions in sub-elements, and the temperature distribution in the coil during the second flux jump. The lower panels show that full flux penetration is achieved in the outer wires while the inner wires are only partially penetrated by the magnetic flux. Furthermore, the temperature is nearly uniform in each

https://doi.org/10.1038/s41467-024-54406-8

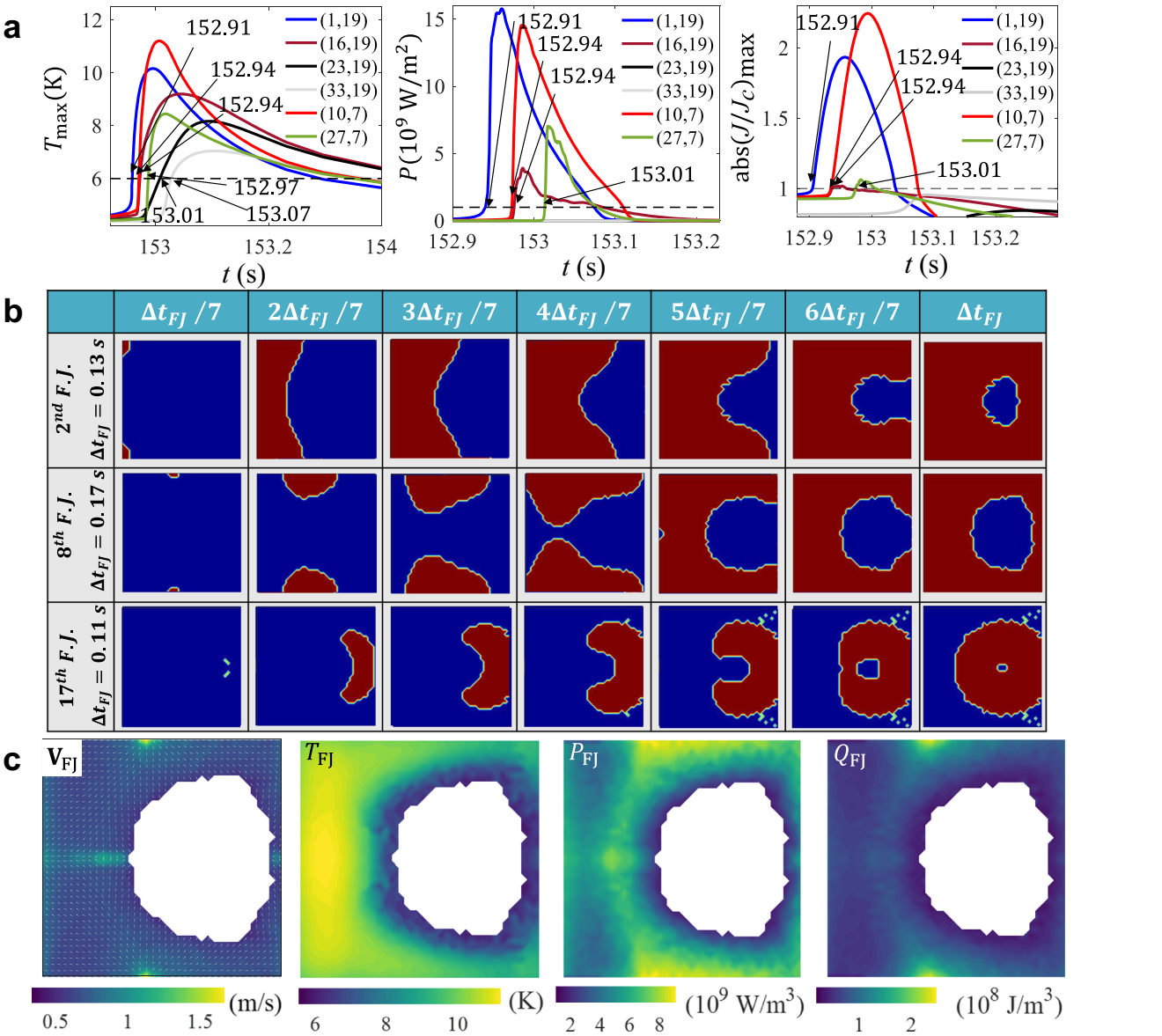

Fig. 4 | Velocity field of a flux jump propagation in a superconducting magnetic coil. a Time evolution of maximum temperature T_{max}, Joule heating power density P, and maximum normalized critical current density **J** of wires at different partial locations during the second flux jump. **b** Snapshots of the time evolution of regions (red color) where the flux jumps occurred. The panels in the last column show the final spatial extent of the flux jumps. **c** Velocity field during the 8th flux jump where the arrows indicate the propagation direction (leftmost panel). The three panels on the right show the temperature T_{FJ} and power density P_{FJ} of each wire at the onset of the 8th flux jump, and the quantity of Joule heating Q_{FJ} generated over a time interval before the occurrence of the 8th flux jump. The data in the white area remains thermomagnetically stable during the 8th flux jump and is represented with numeric data type "not a number" (NaN).

wire, whereas a large temperature gradient can be observed at the border of each wire.

The most fascinating aspect of the phenomenon under consideration concerns the nucleation process of flux jumps and the subsequent growth and propagation throughout the coil. In order to address this question, a criterion is needed to discern whether a thermomagnetic instability has been triggered in one particular wire. As shown in Fig. 4a, the temperature rises in all of the six wires chosen at different locations. However, the time evolution of T does not represent a reliable criterion because the heat conduction from surrounding wires can also lead to a local increase in temperature. As an illustration of this point, in the middle panel of Fig. 4a the Joule heating power density for two wires [(23, 19) and (33, 19)] is plotted. One remark is that the dissipated power is very small during the flux jump process, thus indicating that the flux jump does not occur in these two wires, even though the temperature has increased rapidly. Alternatively, the rightmost panel shows that **J** remains always smaller than J_c in those wires without flux jumps. Based on these considerations, we adopt the criterion $|\mathbf{J}/J_c| > 1$ as the threshold indicating the nucleation of a flux jump.

Figure 4a further indicates that flux jumps do not occur in different wires at the same time. Figure 4b shows the time evolution of the quenched regions where the flux jumps occurred. In this case, the red regions in the rightmost column depict the propagation extent of the 2nd, 8th, and 17th flux jump, while the blue regions remain free of flux jump, which indicates that the flux jump does not propagate into that region. One can see that in an early stage (upper row), the flux jumps are triggered on the left side (corresponding to the inner radius of the coil), while in a later stage, the flux jumps are first observed in the inner wires (lower row). Interestingly, for the latter, the flux jumps do not propagate into the left region of the coil, instead the region of flux jumps remains spatially confined because J_c is weakened by the high magnetic field in the left region. The leftmost panel of Fig. 4c

shows that the propagation velocity field of the 8th flux jump is non-uniform over the coil and lies within a range of 0.3–1.65 m/s. In order to explore what determines the propagation velocity distribution in the coil, we calculated the instantaneous temperature T_{FJ}, the instantaneous Joule heating power density P_{FJ} at the time of $|\mathbf{J}/J_c|$ peak of each wire for the 8th flux jump, and the quantity of Joule heating over a time interval (from an onset time to the flux jump occurrence time) Q_{FJ} in each wire. It is surprising that the propagation velocity of the flux jump from a wire to its neighboring wire is mainly determined by the Q_{FJ} rather than T_{FJ} or P_{FJ}. Our test demonstrates that the onset time has no significant impact on the results if we choose a time interval of 10–30 s. Moreover, the propagation directions of the flux jump are mainly related to the gradient of Q_{FJ}, which indicates that the flux jump of a wire preferably propagates to its neighboring wire with a larger Q_{FJ}. As a consequence, the flux jump ceases its propagation to the wire that does not release sufficient energy. A white area filled with values "NaN" (not a number) indicate this thermomagnetically stable region in Fig. 4c. Animations illustrating the propagation of 2nd, 8th and 17th flux jumps can be seen in the Supplementary Movies 1–3.

Quench propagation in a magnetic coil

Let us now scale up the problem and explore the time evolution of a quenching process in a coil with 20 × 20 turns. To that end, we consider four different cases, each with a progressive increase in complexity. The coil is exposed to a non-uniform self-field generated by a transport current with rate of 2 A/s and a uniform background magnetic field with rate of 15 mT/s. In case 1, the strain effect is neglected in the numerical simulation. In case 2, a constant strain $\varepsilon = 0.5\%$ is taken into consideration for each wire. Real thermal and electromagnetic strain fields with and without pre-strain are considered in cases 3 and 4, respectively. Figure 5a indicates that mechanical strain causes a significant premature quench, likely because strain leads to serious degradation of J_c. Therefore, taking into consideration strain effects is a critical issue for coil design. Indeed, comparing cases 3 and 4, suitable pre-strain by the compression of the aluminum strip can significantly improve the quench current. As shown in Fig. 5b, the current density in all sub-elements exhibits a full current-like state and almost reaches up J_c at the specific time indicated in Fig. 5a. The current density in some sub-elements is still in the field-like state, and thus, these sub-elements still have the capacity to carry more transport current.

The next challenge consists of identifying a reliable indicator for the quench propagation in the coil. As shown in Fig. 6a, the resistivity of each wire increases rapidly to its normal state value ρ_n. Thus, we choose $\rho > 0.95\rho_n$ as the quench criterion for each wire. Figure 6b shows that the onset of quench appears at the center of the left border, and it propagates towards the right border until all wires of the coil switch to the normal state. This numerically predicted behavior of quench propagation shown in Fig. 6b can be validated by a coarse model (see Supplementary Note 12). From Fig. 6c, one can see that the velocity of quench propagation is not uniform in the coil, and the quench propagates much more rapidly in the left region than elsewhere. The simulated velocity of quench propagation is about 0.1–0.45 m/s, which is consistent with the experiments reported in ref. 48. Similar to the case of flux jumps, comparing the velocity field of quench propagation with the time-integration of Joule heating Q_q over a time interval before quench (see Fig. 6f), instantaneous Joule heating power density P_q (Fig. 6e) and instantaneous temperature T_q (Fig. 6d) at quench time, we demonstrate that the propagation velocity of the quenching process is unambiguously correlated to Q_q of each wire. The dynamic propagation of a quench can be found in Supplementary Movie 4.

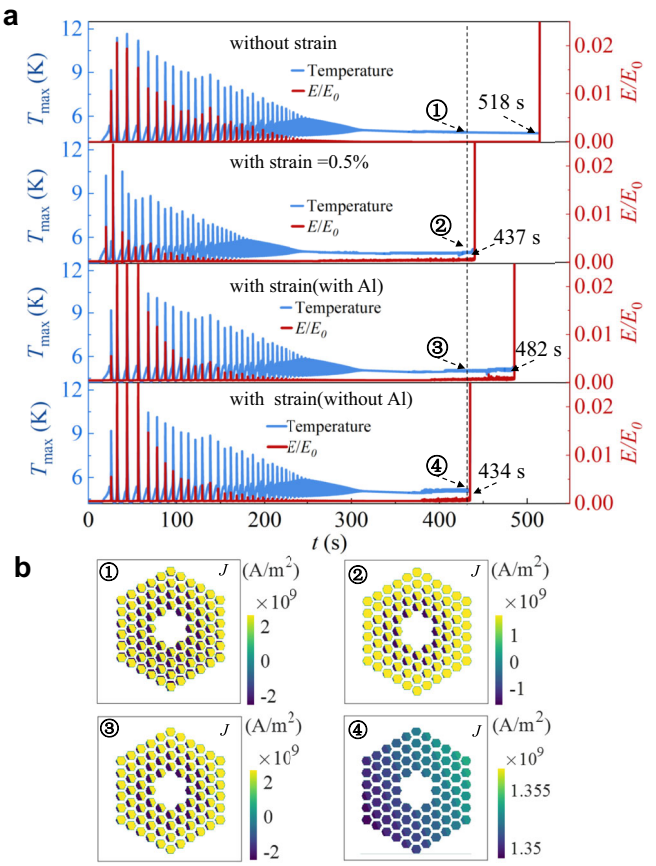

Fig. 5 | Effect of strain on a quench of a solenoid superconducting coil. **a** Simulated variations of the maximum temperature T_{max} (blue) and terminal voltage (red) of a coil with 20 × 20 turns of Nb_3Sn wire for four different cases indicated in each panel. E_0 is the maximum signal during the flux jump phase. **b** The current density distribution in one of the wires of the coil for cases 1–4 at the specific time indicated by the dashed line in panel (**a**).

Discussion

In summary, we have developed a parallel numerical algorithm executed on GPUs permitting to deal with the correlated system of a full-sized solenoid coil with thousand turns of multifilamentary superconducting wires. We have carried out a series of experiments involving magnetization measurements on a short sample of internal-tin Nb_3Sn wires and experimental ramping tests on solenoid coils under different conditions. These experiments were compared with the results of the simulations, thus validating the numerical algorithm for multifilamentary wires and coils.

Utilizing the developed GPU algorithm, we were able to unveil the real-time dynamic and reveal detailed propagating velocity fields of magnetic flux jumps and quenches in superconducting coils. The most striking finding is that the velocity field of the thermomagnetic instability front is mainly related to the quantity of cumulated Joule heating rather than the instantaneous Joule heating power or the maximum temperature. Although the numerical algorithm shown in the main text is intended for solenoid magnets, it can be extended to another structured magnet, such as racetrack coils (see Supplementary Note 15). The large-scale GPU-advanced algorithm lays the foundations for the next generation of numerical superconducting magnet techniques and provides a powerful tool for the optimal design of future high-field magnets, especially those using high-field internal-tin Nb_3Sn wire. Furthermore, it can also find applications in high-temperature superconducting wires/coils with similar structures, such as multifilamentary MgB_2 and Bi2212 wires/coils.

Methods

Experiments

In order to benchmark the numerical calculation against a real superconducting coil, we fabricated two solenoids consisting of 1558

https://doi.org/10.1038/s41467-024-54406-8

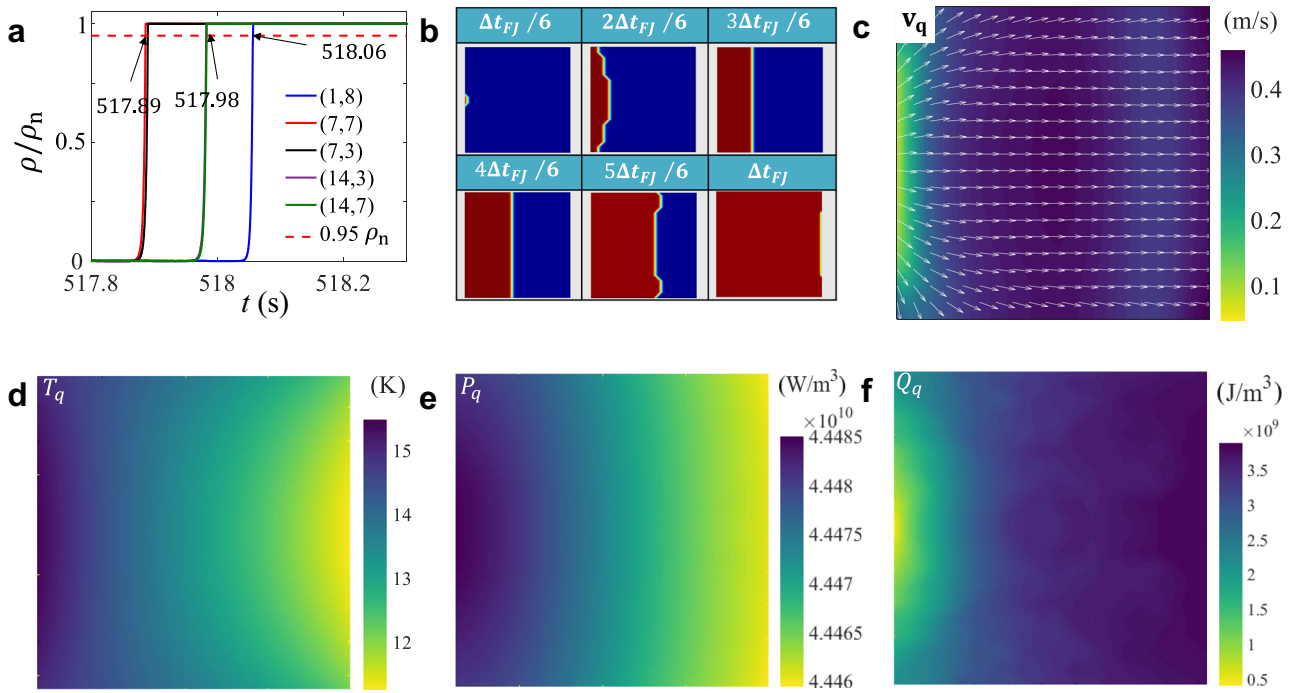

Fig. 6 | Velocity field of a quench propagation in a superconducting magnetic coil. a Resistivity as a function of time during a flux jump at different locations. The criterion of $0.95\rho_n$ used to determine the quenching time for each wire of the coil is indicated with the dashed red line. **b** Time evolution of quenched regions (red colored) at six specific times for case 1 as described in Fig. 5. **c** Velocity field in the coil during the quench with arrows indicating the propagation directions of the quench. **d**–**f** The instantaneous temperature T_q and Joule heating power density P_q of each wire at quench time, and the quantity of Joule heating Q_q of each wire generated over a time interval before quench.

(38 × 41) turns of internal-tin Nb_3Sn wire, as shown in Fig. 1a. The two coils are wound by OST wires and WST wires, respectively (see details in Supplementary Note 3). The diameter of the bare Nb_3Sn wire is 1.3 mm. The OST wire has 84 sub-elements, and the average size of sub-elements is about 110 μm (Fig. 1d). Each sub-element consists of many filaments, which are not drawn in the figure since they coalesce into a single mass. Indeed, for the IT Nb_3Sn wires, the filaments merge to a continuous superconducting region within each sub-element during reactive heat treatment, and thus the effective filament size d_{eff} equals the size of the entire sub-element. In this context, "filament" and "sub-element" are interchangeable terms in this work. The ratio of copper (Cu) to Nb_3Sn is about 1.05 for the OST wire and 0.99 for the WST wire.

Before cooling down to 4.2 K for the experimental test, a pre-stress is applied to the solenoid coils by a thin aluminum strip. The solenoid magnets are then immersed in liquid helium inside a vacuum-insulated Dewar, permitting the bath temperature to be kept at 4.2 K during the experimental tests. Subsequently, the OST and WST solenoid magnets are fed with a transport current under different conditions (see details in Supplementary Notes 3 and 11). The solenoids are only exposed to self-fields without an external magnetic field. The maximum ramping rate of self-field in the coils during the test is about 7 mT/s.

Numerical algorithm

In order to explore the time evolution of thermomagnetic instabilities inside the superconducting coils, we develop a parallel numerical algorithm and execute it on GPUs. In the numerical model, we consider a solenoid coil wound by a multifilamentary superconducting wire (as shown in Fig. 1b), which is exposed to a ramping transport current I_a and a ramping external magnetic field H_a. Due to the rotational symmetry of the solenoid coil, it is sufficient to model a cross-section, as shown in Fig. 1c. Although the wires in real coils are generally arranged into a triangular lattice, for convenience, we chose a geometric model in which the wires are placed in a square lattice, which represents a good approximation to the triangular lattice (see details in Supplementary Note 9).

If a coil is fed with a ramping transport current, each wire simultaneously undergoes a ramping transport current and a concomitant ramping external magnetic field generated by the other wires and coils in its vicinity. As discussed in Supplementary Note 4, the sub-elements in each wire exhibit uncoupled electromagnetic responses for external magnetic field (i.e., they cannot be replaced by an average single conductor) and coupled electromagnetic responses for transport current. Therefore, when a twisted wire with applied current is exposed to a transversal magnetic field, the current density distributions should be in a mixed status between "coupled" and "uncoupled", which is a highly non-trivial problem to implement in the 2D numerical simulations. Not less complex is to consider the cross-talk of stray fields among nearby sub-elements. Figure 2a graphically summarizes the numerical algorithm by introducing a separated A–V method with iterations. It consists of $N_x \times N_y$ turns in which each wire is labeled with a pair of coordinates (i, j) with $i = 1...N_x$ and $j = 1...N_y$. Each wire has N_{sub} sub-elements. Both the turns of the coil and the number of sub-elements are parameters that can be adjusted in the numerical simulations. Figure 2b shows the flow chart for the key subroutine of the numerical algorithm. In order to update the electromagnetic responses of a coil from the time step k to the next time step $k+1$, the wire (i, j), including sub-elements therein, is exposed to an initial uniform magnetic field $\mathbf{H}^{k+1}_{ext,wire}(i,j)$ that is generated from the transport current circulating in the other wires in addition to the background magnetic field, i.e., $\mathbf{H}^{k+1,1}_{ext,sub}(i,j,l) = \mathbf{H}^{k+1}_{ext,wire}(i,j)$ with $l = 1...N_{sub}$. Then, the component of the current density associated with the magnetic field $\mathbf{J}^{k+1,1}_H$ is calculated sub-element after sub-element (one at a time). In addition, the component of current density associated with the transport current $\mathbf{J}^{k+1,1}_I$ distributed in the entire region of a wire with all sub-

elements is calculated by the A–V method. It is worth noting that both $\mathbf{J}_{\mathrm{H}}^{k+1,1}$ and $\mathbf{J}_{\mathrm{I}}^{k+1,1}$ are calculated on the basis of resistivity $\boldsymbol{\rho}^{k}$ as a function of total current density $\mathbf{J}^{k}$ at k time step. The total current density $\mathbf{J}^{k+1,1}=\mathbf{J}_{\mathrm{H}}^{k+1,1}+\mathbf{J}_{\mathrm{I}}^{k+1,1}$, resistivity $\boldsymbol{\rho}^{k+1,1}$ at all grid points and the net current in each sub-element $I_{\mathrm{net}}(i,j,l)$ are then updated. After the first iteration ($m=1$), the external magnetic field $\mathbf{H}_{\mathrm{ext,sub}}^{k+1,2}(i,j,l)$ at each sub-element is updated by the net currents of sub-elements obtained at the first iteration. The second iteration ($m=2$) is performed following a similar procedure as for $m=1$. Such iteration procedure for updating $\mathbf{H}_{\mathrm{ext,sub}}^{k+1,m}(i,j,l)$, $\mathbf{J}_{\mathrm{H}}^{k+1,m}$, $\mathbf{J}_{\mathrm{I}}^{k+1,m}$, $\mathbf{J}^{k+1,m}$ and $\boldsymbol{\rho}^{k+1,m}$ is stopped once the maximum error between the external magnetic field of sub-elements, err, or the error of the Joule heating is sufficiently small. We use an error threshold of 0.1% for the Joule heating and 2.5% for the magnetic field of sub-elements. Eventually, the current density $\mathbf{J}^{k+1}$, resistivity $\boldsymbol{\rho}^{k+1}$ magnetic field $\mathbf{H}^{k+1}$, and Joule heating distribution over the entire cross-section of the coil are obtained for the time step $k+1$. As shown in Fig. S10 of Supplementary Note 4, the convergence of the iteration depends on the number of turns of the coil. Two iterations are sufficiently accurate for small coils ($<10\times10$ turns), and one iteration is good enough for large coils. In order to avoid divergences induced by the strong nonlinear E-J constitutive relation, the Runge–Kutta method with variable time step is implemented to solve the electromagnetic equations.

The constitutive relation between current and electric field for superconductors, $\mathbf{E}=\rho\mathbf{J}$, needs to invoke a nonlinear $\rho(J)$, which is mainly determined by the magnetic flux dynamics. In the past decades, various models describing different flux dynamic regimes have been proposed, such as the Bean critical state model[55], the Anderson–Kim flux creep model[56,57], and the flux-flow model[58,59]. These regimes, spanning from the superconducting state to the normal state, remain a subject of intensive study due to their sensitivity to temperature, strain, current, pinning nature, and magnetic field. A detailed discussion concerning the E-J models is beyond the scope of the present work. Here, we adopt an E-J law[60] able to properly describe the electromagnetic response of superconductors, including the flux creep (FC) state, the flux flow (FF) state and eventually the normal (N) state. In general, the critical current density J_{c} (a parameter entering in the relation $\rho(J)$) also depends strongly on temperature T, strain ε, and magnetic field $\mathbf{H}$. Combining the experimental magnetization loops at various temperatures and transport measurement at 4.2 K (see Supplementary Note 2), we can obtain an accurate dependence of J_{c} on the magnetic field and temperature, as shown in Fig. 2d. The creep exponent n (another parameter in $\rho(J)$) also varies with T and $\mathbf{H}$. The experiments on short samples and the complex E-J dependence with ρ, J_{c}, and n for IT Nb_3Sn are presented in Supplementary Note 2. Additionally, the thermal parameters for Nb_3Sn, copper, and epoxy are described in Supplementary Note 3.

The temperature in the coil at each time step is obtained by the heat diffusion equation $c\frac{\partial T}{\partial t}=\bigtriangledown\cdot(\kappa\bigtriangledown T)+\mathbf{E}\cdot\mathbf{J}$ where $\mathbf{E}\cdot\mathbf{J}$ is the Joule heating source. This equation can be solved by considering the heat exchange boundary conditions at four borders on the cross-section of the coil, $-\kappa(\bigtriangledown T\cdot\mathbf{n})=\mathrm{h}\left(T-T_0\right)$, where c, κ, h are the specific heat, thermal conductivity and heat transfer coefficient, respectively. The thermal parameters are assumed to be proportional to T^3, i.e., $c=c_0\left(T/T_0\right)^3$, $\kappa=\kappa_0\left(T/T_0\right)^3$, $h=h_0\left(T/T_0\right)^3$. The alternating direction implicit (ADI) method is used to solve the heat diffusion equation in the composite coil consisting of Nb_3Sn, copper, and epoxy (further details can be found in Supplementary Notes 8 and 9).

The above numerical algorithm for the coupled electromagnetic equations and heat diffusion equation is realized by a homemade code on C and CUDA programming language, which is executed in parallel on GPUs (see Supplementary Note 13). Details of the flow chart of the main program, the numerical algorithm, the validations of the numerical algorithm, and the parallel processing of the numerical algorithm on GPUs, as well as the computational time and resources for numerical simulations, are presented in Supplementary Notes 4–14.

Data availability

All data supporting the findings of this study are available within the article and its Supplementary Information files or from the corresponding author upon request.

Code availability

Code used for analysis is available at https://doi.org/10.24433/CO.4603770.v1.

References

1. Jeong, S. et al. Voltage spike observation in superconducting cable-in-conduit conductor under ramped magnetic fields: 1. Experiment. *Cryogenics* **37**, 299–304 (1997).
2. Sumption, M. D., Collings, E. W. & Gregory, E. Low field flux jumping in high performance multifilamentary Nb_3Al and Nb_3Sn composite strands. *IEEE Trans. Appl. Supercond.* **9**, 1455–1458 (1999).
3. Sumption, M. D. & Collings, E. W. Stability and flux jumping of internal-Sn, Nb_3Sn conductors (and a model system MgB_2). *IEEE Trans. Appl. Supercond.* **13**, 3394–3397 (2003).
4. Dietderich, D. R. et al. Correlation between strand stability and magnet performance. *IEEE Trans. Appl. Supercond.* **15**, 1524–1528 (2005).
5. Fabbricatore, P. et al. Low-field instabilities in Nb_3Sn multifilamentary wires: the possible role of unreacted Nb. *Supercond. Sci. Technol.* **20**, L34–L37 (2007).
6. Bordini, B., Bottura, L., Oberli, L., Rossi, L. & Takala, E. Impact of the residual resistivity ratio on the stability of Nb_3Sn magnets. *IEEE Trans. Appl. Supercond.* **22**, 4705804 (2012).
7. Bruzzone, P. et al. Collective flux jumps observed during operation of the EDIPO magnets. *IEEE Trans. Appl. Supercond.* **25**, 4701104 (2014).
8. Perez, J. C. et al. 16 T Nb_3Sn racetrack model coil test result. *IEEE Trans. Appl. Supercond.* **26**, 4004906 (2016).
9. Zlobin, A. V. et al. Development and first test of the 15 T Nb_3Sn dipole demonstrator MDPCT1. *IEEE Trans. Appl. Supercond.* **30**, 4000805 (2020).
10. Sun, L. et al. Development of a 1/2-length prototype high field Nb_3Sn magnet for the 4th generation ECR ion source. *Acta Mech. Sin.* **40**, 723376 (2024).
11. Liu, J., Wang, L., Qin, L., Wang, Q. & Dai, Y. Design, fabrication, and test of a 12 T REBCO insert for a 27 T all-superconducting magnet. *IEEE Trans. Appl. Supercond.* **30**, 4300807 (2020).
12. Ghosh, A. K. et al. Dynamic stability threshold in high-performance internal-tin Nb_3Sn superconductors for high field magnets. *Supercond. Sci. Technol.* **18**, L5–L8 (2005).
13. Ghosh, A. K., Cooley, L. D. & Moodenbaugh, A. R. Investigation of instability in high J_c Nb_3Sn strands. *IEEE Trans. Appl. Supercond.* **15**, 3360–3363 (2005).
14. Ambrosio, G. et al. Critical current and instability threshold measurement of Nb_3Sn cables for high field accelerator magnets. *IEEE Trans. Appl. Supercond.* **15**, 1545–1549 (2005).
15. Barzi, E. et al. Instabilities in transport current measurements of Nb_3Sn strands. *IEEE Trans. Appl. Supercond.* **15**, 3364–3367 (2005).
16. Cooley, L. D. More time for Nb_3Sn magnet conductors. *Supercond. Sci. Technol.* **31**, 100501 (2018).
17. Bordini, B. et al. Magnetization measurements of high-J_c Nb_3Sn strands. *IEEE Trans. Appl. Supercond.* **23**, 7100806 (2013).
18. Ballarino, A. & Bottura, L. Targets for R&D on Nb_3Sn conductor for high energy physics. *IEEE Trans. Appl. Supercond.* **25**, 6000906 (2015).

19. Martino, M., Arpaia, P. & Ierardi, S. Impact of flux jumps on high-precision powering of Nb_3Sn superconducting magnets. *J. Phys.: Conf. Ser.* **1350**, 012180 (2019).
20. Kim, Y. B., Hempstead, C. F. & Strnad, A. R. Magnetization and critical supercurrents. *Phys. Rev.* **129**, 528 (1963).
21. Wipf, S. L. & Lubell, M. S. Flux jumping in Nb–25% Zr under nearly adiabatic conditions. *Phys. Lett.* **16**, 103–105 (1965).
22. Wipe, S. L. Magnetic instabilities in type-II superconductors. *Phys. Rev.* **161**, 404 (1967).
23. Swartz, P. S. & Bean, C. P. A model for magnetic instabilities in hard superconductors: the adiabatic critical state. *J. Appl. Phys.* **39**, 4991–4998 (1968).
24. Wipf, S. L. Review of stability in high temperature superconductors with emphasis on flux jumping. *Cryogenics* **31**, 936–948 (1991).
25. Chabanenko, V. V. et al. Magnetothermal instabilities in type II superconductors: the influence of magnetic irreversibility. *J. Appl. Phys.* **88**, 5875–5883 (2000).
26. Mints, R. G. Flux creep and flux jumping. *Phys. Rev. B* **53**, 12311 (1996).
27. Műller, K. H. & Andrikidis, C. Flux jumps in melt-textured Y–Ba–Cu–O. *Phys. Rev. B* **49**, 1294–1307 (1994).
28. Zhou, Y. H. & Yang, X. Numerical simulations of thermomagnetic instability in high-T_c superconductors: dependence on sweep rate and ambient temperature. *Phys. Rev. B* **74**, 054507 (2006).
29. Nabialek, A. et al. Magnetic flux jumps in textured $Bi_2Si_2CaCu_2O_{8+\delta}$. *Phys. Rev. B* **67**, 024518 (2003).
30. Zebouni, N. H., Venkataram, A., Rao, G. N., Grenier, C. G. & Reynolds, J. M. Magnetothermal effects in type II superconductors. *Phys. Rev. Lett.* **13**, 606–609 (1964).
31. Guillot, M. et al. Magnetization jumps and critical current of single crystal. *Phys. Lett. A* **127**, 363–365 (1988).
32. Jiang, L. et al. Selective triggering of magnetic flux avalanches by an edge indentation. *Phys. Rev. B* **101**, 224505 (2020).
33. Wilson, M. N. *Superconducting Magnets* 139–141 (Oxford University Press, Oxford, 1983).
34. Sumption, M. D. & Collings, E. W. Modeling current-field instabilities in high performance Nb_3Sn strands in moderate field. *IEEE Trans. Appl. Supercond.* **17**, 2714 (2007).
35. Kashikhin, V. V. & Zlobin, A. V. Magnetic instabilities in Nb_3Sn strands and cables. *IEEE Trans. Appl. Supercond.* **15**, 1621 (2005).
36. Bordini, B., Barzi, E., Feher, S., Rossi, L. & Zlobin, A. V. Self-field effects in magneto-thermal instabilities for Nb–Sn strands. *IEEE Trans. Appl. Supercond.* **18**, 1309–1312 (2008).
37. Bordini, B. & Rossi, B. L. Self field instability in high-J_c Nb_3Sn strands with high copper residual resistivity ratio. *IEEE Trans. Appl. Supercond.* **19**, 2470–2476, (2009).
38. Bordini, B., Bottura, L., Oberli, L., Rossi, L. & Takala, E. Impact of the residual resistivity ratio on the stability of Nb_3Sn magnets. *IEEE Trans. Appl. Supercond.* **22**, 4705804–4705804 (2012).
39. Cooley, L. D., Chang, P. S. & Ghosh, A. K. Magnetization, RRR and stability of Nb_3Sn strands with high sub-element number. *IEEE Trans. Appl. Supercond.* **17**, 2706–2709 (2007).
40. Ghosh, A. K. Effect of copper resistivity and filament size on the self-field instability of high-J_c Nb_3Sn strands. *IEEE Trans. Appl. Supercond.* **23**, 7100407–7100407 (2013).
41. Ghosh, A. K., Gregory, E. & Peng, X. Stability of high-J_c Nb_3Sn wires in the adiabatic limit. *IEEE Trans. Appl. Supercond.* **21**, 2380–2383 (2010).
42. Sumption, M. D. et al. Critical current density and stability of tube type Nb_3Sn conductors. *Cryogenics* **52**, 91–99 (2012).
43. Sumption, M. D. Stability in Nb_3Sn conductors; magnetic and self-field instability considerations at 4 K and 2 K. *AIP Conf. Proc.* **1219**, 199–207 (2010).
44. Xu, X., Sumption, M. D., Bhartiya, S., Peng, X. & Collings, E. W. Critical current densities and microstructures in rod-in-tube and tube type Nb_3Sn strands-present status and prospects for improvement. *Supercond. Sci. Technol.* **26**, 075015 (2013).
45. Bordini, B. et al. Magneto-thermal stability in LARP Nb_3Sn TQS magnets. *IEEE Trans. Appl. Supercond.* **20**, 274–278 (2010).
46. Takala, E., Bordini, B., Scheuerlein, C. & Rossi, L. Improving Magnetothermal stability in high-J_c Nb_3Sn superconducting strands via the filament cut technique. *IEEE Trans. Appl. Supercond.* **22**, 4706205–4706205 (2012).
47. Rahimzadeh-Kalaleh, S., Ambrosio, G. & Chlachidze, G. et al. Analysis of voltage spikes in superconducting Nb_3Sn magnets. *IEEE Trans. Appl. Supercond.* **19**, 2442–2445 (2009).
48. Bajas, H. et al. Quench analysis of high-current-density Nb_3Sn conductors in racetrack coil configuration. *IEEE Trans. Appl. Supercond.* **25**, 4004005 (2015).
49. Xu, X., Sumption, M. D. & Collings, E. W. Influence of heat treatment temperature and Ti doping on low-field flux jumping and stability in $(Nb–Ta)_3Sn$ strands. *Supercond. Sci. Technol.* **27**, 095009 (2014).
50. Xu, X., Li, P., Zlobin, A. V. & Peng, X. Improvement of stability of Nb_3Sn superconductors by introducing high specific heat substances. *Supercond. Sci. Technol.* **31**, 03LT02 (2018).
51. Wang, Z. et al. Improving superconducting properties of 100 m class MgB_2 wire with 18 + 1 filaments produced via internal Mg diffusion process. *Supercond. Sci. Technol.* **37**, 085017 (2024).
52. Kováš, J., Šouc, J., Kováč, P. & Hušek, I. Magnetization AC losses in MgB_2 wires made by IMD process. *Supercond. Sci. Technol.* **28**, 015013 (2014).
53. Wan, F., Sumption, M. D., Rindfleisch, M. A., Tomsic, M. J. & Collings, E. W. Architecture and transport properties of multifilamentary MgB_2 strands for MRI and low ac loss applications. *IEEE Trans. Appl. Supercond.* **27**, 1–5 (2016).
54. Kwon, H. J. et al. Critical current densities and n-values of MgB_2 conductors for SMES, MRI, and low AC loss applications. *IEEE Trans. Appl. Supercond.* **33**, 1–4 (2023).
55. Bean, C. P. Magnetization of hard superconductors. *Phys. Rev. Lett.* **8**, 250–253 (1962).
56. Kim, Y. B., Hempstead, C. F. & Strand, A. R. Critical persistent currents in hard superconductors. *Phys. Rev. Lett.* **9**, 306–309 (1962).
57. Anderson, P. W. Theory of flux creep in hard superconductors. *Phys. Rev. Lett.* **9**, 309–311 (1962).
58. Feigelman, M. V., Geshkenbein, V. B., Larkin, A. I. & Vinokur, V. M. Theory of collective flux creep. *Phys. Rev. Lett.* **63**, 2303–2306 (1989).
59. Bardeen, J. & Stephen, M. J. Theory of the motion of vortices in superconductors. *Phys. Rev.* **140**, A1197–A1207 (1965).
60. Kramer, E. J. Scaling laws for flux pinning in hard superconductors. *J. Appl. Phys.* **44**, 1360–1370 (1973).

Acknowledgements

C.X. acknowledges support from the National Natural Science Foundation of China (Grant Nos. 12372210 and 11972298) and the Fundamental Research Funds for the Central Universities (lzujbky-2024-jdzx02). L.T.S. acknowledges support from the National Natural Science Foundation of China (11427904, 12025506). The work of A.V.S. was partially supported by the Fonds de la Recherche Scientifique - FNRS under the program EraNet-CHISTERA Grant No. R.8003.21. The authors acknowledge helpful discussions with Prof. You-He Zhou at Lanzhou University, Prof. Benoît Vanderheyden at the University of Liège, and Dr. Peng Ma in Western Superconducting Technologies Co., Ltd.

Author contributions

C.X. designed the research, formulated the idea of the solution, and conceived the main numerical algorithm. H.-X.R and P.J. implemented the numerical simulations, algorithm validation schemes, analyzed the results and Q.-Y.W. performed the mechanical calculations under the supervision of C.X. W.L. prepared the short samples and P.J. implemented experimental measurements for short wires. L.T.S. X.-J.O. and

W.L. fabricated the solenoid coil and implemented measurements. C.X., H.-X.R. prepared the first draft of the manuscript and then improved it with contributions from A.V.S. All authors contributed to discussions and revision of the manuscript to its final version.

Competing interests
The authors declare no competing interests.

Additional information
Supplementary information The online version contains supplementary material available at https://doi.org/10.1038/s41467-024-54406-8.

Correspondence and requests for materials should be addressed to Cun Xue.

Peer review information *Nature Communications* thanks the anonymous reviewer(s) for their contribution to the peer review of this work. A peer review file is available.